

A Mini-Batch Quasi-Newton Proximal Method for Constrained Total-Variation Nonlinear Image Reconstruction

Tao Hong, *Member, IEEE*, Thanh-an Pham, Irad Yavneh, and Michael Unser, *Fellow, IEEE*

Abstract—Over the years, computational imaging with accurate nonlinear physical models has drawn considerable interest due to its ability to achieve high-quality reconstructions. However, such nonlinear models are computationally demanding. A popular choice for solving the corresponding inverse problems is accelerated stochastic proximal methods (ASPMs), with the caveat that each iteration is expensive. To overcome this issue, we propose a mini-batch quasi-Newton proximal method (BQNPM) tailored to image reconstruction problems with total-variation regularization. It involves an efficient approach that computes a weighted proximal mapping at a cost similar to that of the proximal mapping in ASPMs. However, BQNPM requires fewer iterations than ASPMs to converge. We assess the performance of BQNPM on three-dimensional inverse-scattering problems with linear and nonlinear physical models. Our results on simulated and real data show the effectiveness and efficiency of BQNPM.

Index Terms—weighted proximal mapping, second-order, inverse problems, image restoration.

I. INTRODUCTION

THE reconstruction of an image of interest from noisy measurements is a necessary step of many applications such as geophysical, medical, or optical imaging [1]. The measurements are a set $\{\mathbf{y}_\ell \in \mathbb{C}^M\}_{\ell=1}^L$ of L acquired images, while one achieves the reconstruction by solving the composite minimization problem

$$\min_{\mathbf{x} \in \mathcal{C}} \left(\frac{1}{L} \sum_{\ell=1}^L \underbrace{\frac{1}{2} \|\mathcal{H}_\ell(\mathbf{x}) - \mathbf{y}_\ell\|_2^2}_{f_\ell} + \lambda g(\mathbf{x}) \right), \quad (1)$$

where $\mathbf{x} \in \mathbb{R}^N$ is the vectorized image and $\mathcal{C} \subset \mathbb{R}^N$ is a convex set. The data-fidelity terms $\{f_\ell\}_{\ell=1}^L$ ensure consistency with the measurements, the (nonsmooth) regularization term $g(\mathbf{x})$ imposes some prior knowledge on the reconstructed

image, and the tradeoff parameter $\lambda > 0$ balances these two terms. The operator $\mathcal{H}_\ell : \mathbb{R}^N \rightarrow \mathbb{C}^M$ models the physical mapping from the image of interest to the measurements \mathbf{y}_ℓ for $\ell = 1, \dots, L$.

There is a growing interest in accurate physical models, with the hope that they will lead to an increase in the quality of reconstruction. Several imaging modalities have benefited from such refinements; for instance, optical-diffraction tomography (ODT) [2] or full waveform inversion [3]. However, accurate operators \mathcal{H}_ℓ are usually nonlinear and require one to solve some equation in iterative fashion, which comes at a high computational cost due in part to non-convex data-fidelity terms.

The regularization term $g(\mathbf{x})$ plays a key role in the reconstruction of images with suitable properties. There exists a plethora of options, such as the total variation (TV) [4], the Hessian-Schatten norm [5], deep-learning-based techniques [6], plug-and-play (PnP)/regularization by denoising (RED) [7, 8], to name a few. Although recent priors may outperform TV, the latter is still widely used in 3D ODT [9, 10]. This observation motivates us to consider the constrained TV-based reconstruction, which requires us to solve the problem

$$\min_{\mathbf{x} \in \mathcal{C}} \left(\frac{1}{L} \sum_{\ell=1}^L \frac{1}{2} \|\mathcal{H}_\ell(\mathbf{x}) - \mathbf{y}_\ell\|_2^2 + \lambda \text{TV}(\mathbf{x}) \right), \quad (2)$$

where $\text{TV}(\mathbf{x})$ is defined in Section III-B. Many iterative methods have been developed to handle the nonsmoothness of TV [11–15]. In particular, Beck and Teboulle proposed an accelerated proximal method (APM) [15] by using a dual approach [12]. The low computational cost, memory requirements, and fast convergence of APM make it one of the most popular first-order methods.

Quasi-Newton or Newton methods, which use second-order information, require fewer iterations than first-order methods in convex smooth optimization problems [16, 17]. The quasi-Newton proximal methods (QNPMs) are variants adapted to composite problems [18–22]. In [23–25], Ge, Hong *et al.*, and Kadu *et al.* applied QNPMs to solve convex inverse problems with $L = 1$ in x-ray imaging and magnetic resonance imaging, and the nonlinear non-convex inverse-scattering problem with $L > 1$. In their work, the authors observed faster convergence than APMs. However, these deterministic methods still require the computation of the full gradient at each iteration, which can be prohibitive for $L \gg 1$. QNPMs can be seen as first-order methods with a variable metric. This perspective has led

T. Hong and T.-a. Pham contributed equally.

T. Hong is with the Department of Radiology, University of Michigan, Ann Arbor, 48109 USA. (Email: tahong@umich.edu). TH was partly supported by National Institutes of Health grant R01NS112233.

T.-a. Pham was with the Biomedical Imaging Group, Ecole polytechnique fédérale de Lausanne, Lausanne, Switzerland. He is now with the 3D Optical Systems Group, Department of Mechanical Engineering, Massachusetts Institute of Technology, 77 Massachusetts Ave, Cambridge, Massachusetts 02139, USA. (Email: tampham@mit.edu).

I. Yavneh is with the Department of Computer Science, Technion-Israel Institute of Technology, Haifa, 3200003 Israel. (Email: irad@cs.technion.ac.il).

M. Unser is with the Biomedical Imaging Group, Ecole polytechnique fédérale de Lausanne, Lausanne, Switzerland. (Email: michael.unser@epfl.ch).

to another class of algorithms called variable metric operator splitting methods (VMOSMs) [26–28]. We refer the reader to the prior work section in [21], where Becker *et al.* extensively discussed the differences between QNPMs and VMOSMs.

Stochastic methods are efficient iterative algorithms that mitigate the computational burden when $L \gg 1$. These methods estimate the gradient from a (varying) subset of $\{f_\varrho\}_{\varrho=1}^L$ at each iteration [29–32], making the computational cost independent of L . The stochastic counterpart of APMs has been used in many instances of image reconstruction [2, 33, 34]. Thus, stochastic or mini-batch second-order methods were proposed. Their most challenging part is the estimation of the Hessian matrix from a noisy gradient. To address this difficulty, variance-reduction techniques have proven to be effective [35–38]. Other methods [38–40] were proposed to address the nonconvex settings. Wang *et al.* [41] extended the variance-reduced stochastic quasi-Newton methods to solve composite problems with $g(\mathbf{x}) = \|\mathbf{x}\|_1$ and non-convex $\{f_\varrho\}_{\varrho=1}^L$. However, these methods still require the evaluation of the full gradient at some regular intervals during the optimization. When the number of data-fidelity terms is large, this can be computationally prohibitive. All these aspects hinder the deployment of quasi-Newton methods to large-scale imaging modalities such as 3D ODT, where L is large and the physical model is nonlinear.

II. CONTRIBUTIONS AND ROADMAPS

In this work, we derive a *mini-batch quasi-Newton proximal method* (BQNPM) that never requires the evaluation of the full gradient and converges faster than accelerated stochastic proximal methods (ASPMs) in terms of the number of iterations and wall time. BQNPM requires one to compute a weighted proximal mapping (WPM) (defined in Section III-D) at each iteration, which appears to be as challenging as the original problem. In [23, 25], the WPM is computed with first-order methods such as FISTA or primal-dual methods. Their algorithm involves inner and outer iterations, which adds to the global complexity (*i.e.*, a three-layered iterative optimization). Here instead, we consider a *constrained* TV-based image reconstruction and leverage the dual formulation of TV, in a way similar to the seminal work of Beck and Teboulle [15]. By doing so, we can use the fast dual projected-gradient method to compute the WPM. This avoids the embedding of additional iterative algorithms and ensures fast convergence. Although the proposed computation of WPM is similar to the one described in [24], we tackle a constrained WPM (*i.e.*, $\mathbf{x} \in \mathcal{C}$) in the context of a mini-batch second-order method and a nonlinear non-convex inverse problem. This introduces new challenges, as shown in (13), where \mathbf{B}^k is neither an identity matrix nor a diagonal matrix. Furthermore, we employ a memory-friendly symmetric rank-1 method to reduce memory usage in estimating the Hessian matrices. Our results show that our method requires fewer iterations and less computation time than first-order methods to achieve a satisfactory quality of reconstruction. Our method is thus suitable to large-scale and nonlinear inverse problems.

The paper is organized as follows: In Section III, we set the notation and introduce preliminaries. In Section IV, we

derive the proposed BQNPM and present some implementation details. In Section V, we study the performance of our method on three-dimensional inverse-scattering problems with simulated and real data.

III. PRELIMINARIES

In this section, we set the notation and present the discretized form of TV and its dual representation. We then introduce the definition of the WPM and some necessary properties.

A. Notations

For a matrix $\mathbf{X} \in \mathbb{R}^{I \times J}$, the notation $\text{vec}(\mathbf{X})$ stands for its vectorized version $\mathbf{x} \in \mathbb{R}^{IJ}$. Similarly, for a vectorized image $\mathbf{x} \in \mathbb{R}^N$, the notation $\text{MAT}(\mathbf{x}) = \mathbf{X} \in \mathbb{R}^{I \times J}$ denotes its matrix form. The (r, c) th (n)th element of a matrix $\mathbf{X} \in \mathbb{R}^{I \times J}$ (vector $\mathbf{x} \in \mathbb{R}^N$) is represented as $X_{r,c}$ (x_n , respectively). The $(N \times N)$ identity matrix is denoted by \mathbf{I}_N . The notation $\langle \cdot, \cdot \rangle$ stands for the inner product.

Let $N = \prod_{n=1}^d K_n$ be the product of the lengths of the sides of some d -dimensional array a . For $k_n \in [0 \dots K_n - 1]$, the vectorized data $\mathbf{x} \in \mathbb{R}^N$ satisfy

$$a[k_1, k_2, \dots, k_d] = x_{1 + \sum_{n=1}^d k_n K'_n},$$

where $K'_1 = 1$ and $K'_n = K'_{n-1} K_{n-1}$. For $r, c \in [1 \dots N]$, the finite-difference matrix \mathbf{D}^n along the n th dimension is made of general components

$$d_{r,c}^n = -\delta[c - r] + \delta[c - r - K'_n],$$

up to the Neumann boundary conditions characterized by $d_{r,c}^n = 0$ whenever $\lceil r/K'_n \rceil \in K_n \mathbb{N}$.

B. Discretized Total Variation

We present two popular variants of TV: isotropic and anisotropic [4]. The isotropic discretized total variation of \mathbf{x} is defined as

$$\text{TV}_{\text{iso}}(\mathbf{x}) = \text{tr} \left(\sqrt{\sum_{n=1}^d (\mathbf{D}^n \mathbf{x}) (\mathbf{D}^n \mathbf{x})^\top} \right), \quad (3)$$

while the anisotropic version is defined as

$$\text{TV}_{\ell_1}(\mathbf{x}) = \text{tr} \left(\sum_{n=1}^d \sqrt{(\mathbf{D}^n \mathbf{x}) (\mathbf{D}^n \mathbf{x})^\top} \right), \quad (4)$$

where \top represents the transpose operator. In (3) and (4), the square root must be understood component-wise.

C. Dual Representation of Total Variation

From the observation that

$$\|\mathbf{x}\| = \max_{\mathbf{z} \in \mathbb{R}^N, \|\mathbf{z}\|_* \leq 1} \mathbf{z}^\top \mathbf{x},$$

where $\|\cdot\|_*$ denotes the dual norm of $\|\cdot\|$, Chambolle deduced in [12] that (3) and (4) may be rewritten as

$$\text{TV}_{\text{iso}}(\mathbf{x}) = \max_{\mathbf{P} \in \mathbb{R}^{d \times N}, \{\|\mathbf{c}_k\|_2 \leq 1\}_{k=1}^N} \mathbf{d}(\mathbf{P})^\top \mathbf{x} \quad (5)$$

TABLE I
NOTATIONS USED IN THE DERIVATION OF THE MINI-BATCH
QUASI-NEWTON PROXIMAL METHOD.

K_s	Total number of subsets
\mathbf{x}_{k-t}	Iterate at the $(k-t)$ th iteration
$\kappa(k, t)$	Subset index at the k th iteration for the t th term in (12): $\kappa(k, t) = \text{mod}(k-1-t, K_s) + 1 \in [1, K_s]$
$\nabla F_{\kappa(k,t)}(\mathbf{x}_{k-t})$	Gradient associated with the $\kappa(k, t)$ th subset
$\mathbf{B}_{k-t}^{\kappa(k,t)}$	Estimated Hessian matrix associated with the $\kappa(k, t)$ th subset (computed with Algorithm 3)

and

$$\text{TV}_{\ell_1}(\mathbf{x}) = \max_{\mathbf{P} \in \mathbb{R}^{d \times N}, \{\|\mathbf{c}_k\|_\infty \leq 1\}_{k=1}^N} \mathbf{d}(\mathbf{P})^\top \mathbf{x}, \quad (6)$$

respectively. Further, the $(d \times N)$ matrix

$$\mathbf{P} = [\mathbf{c}_1 \cdots \mathbf{c}_N] = [\mathbf{r}_1 \cdots \mathbf{r}_d]^\top$$

contains the variables over which the maximization is performed. Furthermore, the vector-valued function $\mathbf{d} : \mathbb{R}^{d \times N} \rightarrow \mathbb{R}^N$ is given by

$$\mathbf{d}(\mathbf{P}) = \sum_{n=1}^d (\mathbf{D}^n)^\top \mathbf{r}_n.$$

D. Weighted Proximal Mapping

Definition 1 (Weighted proximal mapping). *Given a proper closed convex function $g(\mathbf{x})$ and a symmetric positive-definite matrix $\mathbf{W} \succ 0 \in \mathbb{R}^{N \times N}$, the WPM associated with g is defined as*

$$\text{prox}_g^{\mathbf{W}}(\mathbf{x}) = \arg \min_{\mathbf{u} \in \mathbb{R}^N} \left(g(\mathbf{u}) + \frac{1}{2} \|\mathbf{u} - \mathbf{x}\|_{\mathbf{W}}^2 \right), \quad (7)$$

where $\|\mathbf{x}\|_{\mathbf{W}} \triangleq \sqrt{\mathbf{x}^\top \mathbf{W} \mathbf{x}}$ denotes the \mathbf{W} -norm.

For $\mathbf{W} = \mathbf{I}_N$, (7) corresponds to the well-known proximal mapping [42] and has a closed-form solution for many popular g .¹ Next, we outline some properties of (7):

- (1) The $\text{prox}_g^{\mathbf{W}}(\mathbf{x})$ exists and is unique for $\mathbf{x} \in \mathbb{R}^N$ since $g(\mathbf{u}) + \frac{1}{2} \|\mathbf{u} - \mathbf{x}\|_{\mathbf{W}}^2$ is strongly convex.
- (2) Denote

$$g^{\mathbf{W}}(\mathbf{x}) = \inf_{\mathbf{u} \in \mathbb{R}^N} \left(g(\mathbf{u}) + \frac{1}{2} \|\mathbf{u} - \mathbf{x}\|_{\mathbf{W}}^2 \right).$$

The function $g^{\mathbf{W}}(\mathbf{x})$ is continuously differentiable on \mathbb{R}^N with gradient

$$\nabla g^{\mathbf{W}} = \mathbf{W}(\mathbf{x} - \text{prox}_g^{\mathbf{W}}(\mathbf{x})) \quad (8)$$

and Lipschitz constant $\omega_{\mathbf{W}}$, where $\omega_{\mathbf{W}}$ is the largest eigenvalue of \mathbf{W} .

For further details of WPM, we refer the reader to [19, 21].

The proximal mapping has a closed-form solution for many popular g [43, Chapter 6]. Although this does not necessarily carry over to $\text{prox}_g^{\mathbf{W}}(\mathbf{x})$ with a generic \mathbf{W} , the computation of $\text{prox}_g^{\mathbf{W}}(\mathbf{x})$ can be simplified when $\mathbf{W} = \Sigma \pm \mathbf{U}\mathbf{U}^\top$ (Theorem 1), where $\Sigma \in \mathbb{R}^{N \times N}$ is a diagonal matrix and $\mathbf{U} \in \mathbb{R}^{N \times r}$ is rank- r matrix with $r \ll N$.

Theorem 1. [21, Theorem 3.4] *Let $\mathbf{W} = \Sigma \pm \mathbf{U}\mathbf{U}^\top$, $\mathbf{W} \succ 0 \in \mathbb{R}^{N \times N}$, and $\mathbf{U} \in \mathbb{R}^{N \times r}$. Then, it holds that*

$$\text{prox}_g^{\mathbf{W}}(\mathbf{x}) = \text{prox}_g^{\Sigma}(\mathbf{x} \mp \Sigma^{-1} \mathbf{U} \beta^*), \quad (9)$$

where $\beta^* \in \mathbb{R}^r$ is the unique solution of the nonlinear system of equation

$$\underbrace{\mathbf{U}^\top (\mathbf{x} - \text{prox}_g^{\Sigma}(\mathbf{x} \mp \Sigma^{-1} \mathbf{U} \beta))}_{\varphi(\beta)} + \beta = \mathbf{0}. \quad (10)$$

Because Σ is a diagonal matrix, the computation of $\text{prox}_g^{\Sigma}(\mathbf{x})$ is as simple as the proximal mapping associated with g . To solve (10), we use a semi-smooth Newton method [44], assuming that r is small. In practice, we find that a few iterations are sufficient to obtain an accurate solution. In Section IV-B, we provide more details about our implementation of the semi-smooth Newton method.

IV. PROPOSED MINI-BATCH QUASI-NEWTON PROXIMAL METHOD

In this section, we derive BQNPM for solving (2). We first split the index set $\{1, 2, \dots, L\}$ into K_s subsets $\{\mathcal{S}_t\}_{t=1}^{K_s}$ and then rewrite (2) as

$$\min_{\mathbf{x} \in \mathcal{C}} \left(\frac{1}{K_s} \sum_{t=1}^{K_s} F_t(\mathbf{x}) + \lambda \text{TV}(\mathbf{x}) \right), \quad (11)$$

where $F_t(\mathbf{x}) = \frac{1}{|\mathcal{S}_t|} \sum_{\rho \in \mathcal{S}_t} f_\rho(\mathbf{x})$ and $L = \sum_{t=1}^{K_s} |\mathcal{S}_t|$, with $|\mathcal{S}_t|$ denoting the cardinality of \mathcal{S}_t . Note that $|\mathcal{S}_t|$ can be different for each t . For the sake of brevity, we now write $\sum_{t=1}^{K_s}$ as \sum_t . Inspired by [45], BQNPM computes \mathbf{x}_k at iteration $k > K_s$ by taking advantage of the local second-order Taylor approximations of $F_t, \forall t$

$$\begin{aligned} \mathbf{x}_k = \arg \min_{\mathbf{x} \in \mathcal{C}} & \left(\sum_t \left(\langle \nabla F_{\kappa(k,t)}(\mathbf{x}_{k-t}), \mathbf{x} - \mathbf{x}_{k-t} \rangle \right. \right. \\ & \left. \left. + \frac{1}{2a_k} (\mathbf{x} - \mathbf{x}_{k-t})^\top \mathbf{B}_{k-t}^{\kappa(k,t)} (\mathbf{x} - \mathbf{x}_{k-t}) \right) \right. \\ & \left. + K_s \lambda \text{TV}(\mathbf{x}) \right), \end{aligned} \quad (12)$$

where $\kappa(k, t) = \text{mod}(k-1-t, K_s) + 1$ assigns the appropriate subset, $a_k > 0$ is the stepsize, and $\mathbf{B}_{k-t}^{\kappa(k,t)} \succ 0$ is the estimated Hessian matrix associated with $F_{\kappa(k,t)}$ at the k th iteration. Note that the Taylor approximations are done at a different point for each subset. These points are the K_s previous iterates and their assigned subset is defined by $\kappa(k, t)$.

At each iteration, we only have to update the gradient and (estimated) Hessian matrix of the subset associated with iterate \mathbf{x}_{k-1} . This is because the other entries were already computed (and saved) in the previous iterations. To do so,

¹<http://proximity-operator.net/>

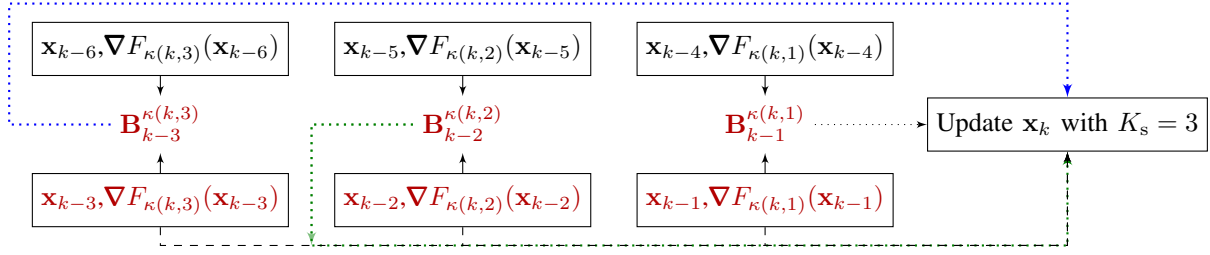


Fig. 1. Flowchart of the iterates, gradients, and Hessian matrices of (12) at the k th iteration with $K_s = 3$.

BQNPM incorporates a cycling routine which only computes quantities over one subset per iteration. To obtain second-order information, we also estimate the Hessian matrices in a cycling fashion (see Section IV-A). We display in Fig. 1 the iterates, gradients, and Hessian matrices used in (12) with $K_s = 3$ and list in Table I the key notations used in this work.

The optimization problem in (12) corresponds to a WPM. We can rewrite it as

$$\mathbf{x}_k = \arg \min_{\mathbf{x} \in \mathcal{C}} \left(\frac{1}{2} \|\mathbf{x} - \mathbf{v}_k\|_{\mathbf{B}^k}^2 + a_k K_s \lambda \text{TV}(\mathbf{x}) \right), \quad (13)$$

where we have introduced $\mathbf{B}^k = \sum_t \mathbf{B}_{k-t}^{\kappa(k,t)}$ and $\mathbf{v}_k = (\mathbf{B}^k)^{-1} \sum_t (\mathbf{B}_{k-t}^{\kappa(k,t)} \mathbf{x}_{k-t} - a_k \nabla F_{\kappa(k,t)}(\mathbf{x}_{k-t}))$. For $\mathbf{B}_{k-t}^{\kappa(k,t)} = \mathbf{I}_N, \forall t$, (13) degenerates to the proximal mapping, which can be solved efficiently with the fast dual proximal method proposed by Beck and Teboulle [15]. In our case, $\mathbf{B}_{k-t}^{\kappa(k,t)} \neq \mathbf{I}_N, \forall t$, and we have to compute a nontrivial WPM. Our method is inspired by [15]. Using the dual form of the TV function given in (5) or (6), we rewrite (13) as

$$\min_{\mathbf{x} \in \mathcal{C}} \left(\max_{\mathbf{P} \in \mathcal{P}} \frac{1}{2} \|\mathbf{x} - \mathbf{v}_k\|_{\mathbf{B}^k}^2 + a_k K_s \lambda \mathbf{d}(\mathbf{P})^\top \mathbf{x} \right), \quad (14)$$

where $\mathcal{P} = \left\{ \mathbf{P} \in \mathbb{R}^{d \times N} : \{\|\mathbf{c}_k\|_2 \leq 1\}_{k=1}^N \right\}$ for the isotropic TV and $\mathcal{P} = \left\{ \mathbf{P} \in \mathbb{R}^{d \times N} : \{\|\mathbf{c}_k\|_\infty \leq 1\}_{k=1}^N \right\}$ for the anisotropic TV.

By reorganizing (14), we extract the problem

$$\min_{\mathbf{x} \in \mathcal{C}} \max_{\mathbf{P} \in \mathcal{P}} \|\mathbf{x} - \mathbf{w}_k(\mathbf{P})\|_{\mathbf{B}^k}^2 - \|\mathbf{w}_k(\mathbf{P})\|_{\mathbf{B}^k}^2, \quad (15)$$

where $\mathbf{w}_k(\mathbf{P}) = \mathbf{v}_k - a_k K_s \lambda (\mathbf{B}^k)^{-1} \mathbf{d}(\mathbf{P})$. Since (15) is convex in \mathbf{x} and concave in \mathbf{P} , we can interchange the min and the max to obtain

$$\max_{\mathbf{P} \in \mathcal{P}} \min_{\mathbf{x} \in \mathcal{C}} \|\mathbf{x} - \mathbf{w}_k(\mathbf{P})\|_{\mathbf{B}^k}^2 - \|\mathbf{w}_k(\mathbf{P})\|_{\mathbf{B}^k}^2. \quad (16)$$

Let

$$\delta_{\mathcal{C}}(\mathbf{x}) = \begin{cases} 0, & \mathbf{x} \in \mathcal{C} \\ \infty, & \mathbf{x} \notin \mathcal{C}. \end{cases} \quad (17)$$

Since \mathbf{x} only appears in the first term of (16), the optimal solution of \mathbf{x} in (16) is the WPM associated with $\delta_{\mathcal{C}}(\mathbf{x})$, *i.e.*,

$$\mathbf{x}^* = \text{prox}_{\delta_{\mathcal{C}}}^{\mathbf{B}^k}(\mathbf{w}_k(\mathbf{P})). \quad (18)$$

Substituting (18) into (16), we obtain a dual problem that now involves the dual variables

$$\mathbf{P}^* = \arg \min_{\mathbf{P} \in \mathcal{P}} \left(-\|\mathbf{w}_k(\mathbf{P}) - \text{prox}_{\delta_{\mathcal{C}}}^{\mathbf{B}^k}(\mathbf{w}_k(\mathbf{P}))\|_{\mathbf{B}^k}^2 + \|\mathbf{w}_k(\mathbf{P})\|_{\mathbf{B}^k}^2 \right). \quad (19)$$

The primal variable \mathbf{x}_k is then given by

$$\mathbf{x}_k = \text{prox}_{\delta_{\mathcal{C}}}^{\mathbf{B}^k}(\mathbf{w}_k(\mathbf{P}^*)).$$

Since the objective function of (19) is convex and continuously differentiable, we can simply apply an APM. The gradient and Lipschitz constant of (19) are proposed in Lemma 1. The whole algorithm that solves (12) is summarized in Algorithm 2.

Algorithm 1 Proposed mini-batch quasi-Newton proximal method.

Initialization: Initial guess $\mathbf{x}_0 \in \mathbb{R}^N$; tradeoff parameter λ ; number K_s of sets; sets $\{\mathcal{S}_t\}_{t=1}^{K_s}$; stepsize $a_k = 1$; Lipschitz constants α_t of $F_t, \forall t$; maximal number of iterations `Max_Iter`.

Output: \mathbf{x}^*

- 1: $k \leftarrow 1$
 - 2: **for all** $k \leq \text{Max_Iter}$ **do**
 - 3: **if** $k \leq K_s$ **then**
 - 4: Evaluate $\nabla F_{\kappa(k,1)}(\mathbf{x}_{k-1})$
 - 5: $\mathbf{B}_{k-1}^{\kappa(k,1)} = \alpha_{\kappa(k,1)} \mathbf{I}_N$
 - 6:
$$\mathbf{x}_k = \arg \min_{\mathbf{x} \in \mathcal{C}} \left(\nabla F_{\kappa(k,1)}(\mathbf{x}_{k-1})^\top (\mathbf{x} - \mathbf{x}_{k-1}) + \frac{1}{2a_k} (\mathbf{x} - \mathbf{x}_{k-1})^\top \mathbf{B}_{k-1}^{\kappa(k,1)} (\mathbf{x} - \mathbf{x}_{k-1}) + \lambda \text{TV}(\mathbf{x}) \right)$$
 - 7: **else**
 - 8: Evaluate $\nabla F_{\kappa(k,1)}(\mathbf{x}_{k-1})$ and estimate $\mathbf{B}_{k-1}^{\kappa(k,1)}$ with Algorithm 3
 - 9: Compute \mathbf{P}^* with Algorithm 2
 - 10: Compute $\mathbf{x}_k = \text{prox}_{\delta_{\mathcal{C}}}^{\mathbf{B}^k}(\mathbf{w}_k(\mathbf{P}^*))$ using Theorem 1 and Algorithm 4
 - 11: **end if**
 - 12: Store \mathbf{x}_{k-1} , $\nabla F_{\kappa(k,1)}(\mathbf{x}_{k-1})$, and $\mathbf{B}_{k-1}^{\kappa(k,1)}$
 - 13: $k \leftarrow k + 1$
 - 14: **end for**
 - 15: **return** $\mathbf{x}^* \leftarrow \mathbf{x}_{\text{Max_Iter}}$
-

Lemma 1. *The gradient of the objective function in (19) is*

$$-2a_k K_s \lambda \mathbf{d} \left(\text{prox}_{\delta_C}^{\mathbf{B}^k} (\mathbf{w}_k(\mathbf{P})) \right), \quad (20)$$

with Lipschitz constant $16\omega_{\min}^k a_k^2 K_s^2 \lambda^2$ (or $24\omega_{\min}^k a_k^2 K_s^2 \lambda^2$) for 2D (or 3D), where ω_{\min}^k is the smallest eigenvalue of \mathbf{B}^k .

Proof. We provide the proof in Appendix A. \square

Algorithm 2 Efficient solver for the duality of (12) (i.e., (19)).

Initialization: $\{\mathbf{B}_{k-t}^{\kappa(k,t)}\}_{t=1}^{K_s}$; $\{\mathbf{x}_{k-t}\}_{t=1}^{K_s}$; a_k ; $K_s \lambda$; the last \mathbf{P}^* ; maximal number of iterations Max_Iter; tolerance ϵ .

- 1: $\mathbf{B}^k = \sum_t \mathbf{B}_{k-t}^{\kappa(k,t)}$
- 2: Iter $\leftarrow 1$
- 3: $\mathbf{P}_{\text{Iter}} \leftarrow \mathbf{P}^*$
- 4: $\bar{\mathbf{P}}_{\text{Iter}} \leftarrow \mathbf{P}^*$
- 5: $t_{\text{Iter}} \leftarrow 1$
- 6: **for all** Iter \leq Max_Iter **do**
- 7: Compute $\mathbf{Q}_{\text{Iter}} = \text{prox}_{\delta_C}^{\mathbf{B}^k} (\mathbf{w}_k(\bar{\mathbf{P}}_{\text{Iter}}))$ using Theorem 1 and Algorithm 4
- 8: $\mathbf{P}_{\text{Iter}+1} \leftarrow \bar{\mathbf{P}}_{\text{Iter}} + \frac{1}{12\omega_{\min}^k a_k K_s \lambda} \mathbf{d}(\mathbf{Q}_{\text{Iter}})$
- 9: **if** $\frac{\|\mathbf{P}_{\text{Iter}+1} - \mathbf{P}_{\text{Iter}}\|}{\|\mathbf{P}_{\text{Iter}}\|} < \epsilon$ **then**
- 10: **break**
- 11: **else**
- 12: $t_{\text{Iter}+1} \leftarrow \frac{1 + \sqrt{1 + 4t_{\text{Iter}}^2}}{2}$
- 13: $\bar{\mathbf{P}}_{\text{Iter}+1} \leftarrow \mathbf{P}_{\text{Iter}+1} + \frac{t_{\text{Iter}} - 1}{t_{\text{Iter}+1}} (\mathbf{P}_{\text{Iter}+1} - \mathbf{P}_{\text{Iter}})$
- 14: Iter \leftarrow Iter + 1
- 15: **end if**
- 16: **end for**
- 17: **return** $\mathbf{P}^* \leftarrow \mathbf{P}_{\text{Iter}+1}$

For a generic \mathbf{B}^k , (19) is computationally prohibitive. The main bottleneck resides in the computation of $\mathbf{w}_k(\mathbf{P})$ and $\text{prox}_{\delta_C}^{\mathbf{B}^k} (\mathbf{w}_k(\mathbf{P}))$ in (20). To circumvent this issue, we enforce that our estimated Hessian matrices are of the form $\alpha \mathbf{I}_N + \mathbf{u}\mathbf{u}^\top$ with an adequate $\alpha > 0$ and $\mathbf{u} \in \mathbb{R}^N$ (Section IV-A). As we shall see in Section IV-B, this trick renders the computation of $\mathbf{w}_k(\mathbf{P})$ and $\text{prox}_{\delta_C}^{\mathbf{B}^k} (\mathbf{w}_k(\mathbf{P}))$ inexpensive. The steps of BQNPM are summarized in Algorithm 1 with some further details below.

- For $k \leq K_s$, we set $\mathbf{B}^k = \mathbf{B}_{k-1}^{\kappa(k,1)}$, so that only the subset $\mathcal{S}_{\kappa(k,1)}$ is involved (lines 3-6). For $k > K_s$, we compute \mathbf{x}_k by solving (14) with $\mathbf{B}^k = \sum_t \mathbf{B}_{k-t}^{\kappa(k,t)}$ (lines 8-10).
- In contrast to the ASPMs, BQNPM needs more memory to save the latest K_s iterates, gradients, and estimated Hessian matrices. It is noteworthy that our estimated Hessian matrices only require us to store a vector per subset (see Algorithm 3). BQNPM then requires extra memory for saving $3K_s$ additional images.

A. Estimation of the Hessian Matrix

By construction, the proposed method requires one to estimate the Hessian matrix $\mathbf{B}_{k-1}^{\kappa(k,1)}$ at each iteration. For that purpose, we deploy the *symmetric-rank-1* (SR1) method [16], whose implementation is summarized in Algorithm 3. The

classical SR1 method uses the previously estimated Hessian matrix with a rank-1 correction. Here, by contrast, we enforce that $\mathbf{B}_{k-1}^{\kappa(k,1)} = \tau_k^{\kappa(k,1)} \mathbf{I}_N + \mathbf{u}_{k-1}^{\kappa(k,1)} (\mathbf{u}_{k-1}^{\kappa(k,1)})^\top$, so that in practice we only need to store a scalar $\tau_k^{\kappa(k,1)} > 0$ and a vector $\mathbf{u}_{k-1}^{\kappa(k,1)} \in \mathbb{R}^N$ for each subset [21].

Algorithm 3 SR1 estimation: $\mathbf{B}_{k-1}^{\kappa(k,1)}$

Initialization:

- $\mathbf{s}_k = \mathbf{x}_{k-1} - \mathbf{x}_{k-1-K_s}$,
- $\mathbf{m}_k = \nabla F_{\kappa(k,1)}(\mathbf{x}_{k-1}) - \nabla F_{\kappa(k,1)}(\mathbf{x}_{k-1-K_s})$, $\gamma \in (0, 1)$,
- and $\alpha_{\kappa(k,1)}$.
- Output:** $\mathbf{B}_{k-1}^{\kappa(k,1)}$
- 1: $\tau \leftarrow \gamma \frac{\langle \mathbf{m}_k, \mathbf{m}_k \rangle}{\langle \mathbf{s}_k, \mathbf{m}_k \rangle}$.
- 2: **if** $\tau < 0$ **then**
- 3: $\tau \leftarrow \alpha_{\kappa(k,1)}$
- 4: $\mathbf{B}_{k-1}^{\kappa(k,1)} = \tau \mathbf{I}_N$
- 5: **else**
- 6: $\mathbf{B}_0 \leftarrow \tau \mathbf{I}_N$
- 7: **if** $\langle \mathbf{m}_k - \mathbf{B}_0 \mathbf{s}_k, \mathbf{s}_k \rangle \leq 10^{-8} \|\mathbf{s}_k\|_2 \|\mathbf{m}_k - \mathbf{B}_0 \mathbf{s}_k\|_2$ **then**
- 8: $\mathbf{u} \leftarrow 0$
- 9: **else**
- 10: $\mathbf{u} \leftarrow \frac{\mathbf{m}_k - \mathbf{B}_0 \mathbf{s}_k}{\sqrt{\langle \mathbf{m}_k - \mathbf{B}_0 \mathbf{s}_k, \mathbf{s}_k \rangle}}$
- 11: **end if**
- 12: $\mathbf{B}_{k-1}^{\kappa(k,1)} = \mathbf{B}_0 + \mathbf{u}\mathbf{u}^\top$
- 13: $\mathbf{u}_{k-1}^{\kappa(k,1)} = \mathbf{u}$
- 14: **end if**
- 15: $\tau_{k-1}^{\kappa(k,1)} = \tau$

B. Implementation Details

To compute $\mathbf{w}_k(\mathbf{P})$, we have to invert \mathbf{B}^k . Since $\{\mathbf{B}_{k-t}^{\kappa(k,t)}\}_{t=1}^{K_s}$ is a set of rank-1 corrected matrices, we have that

$$\mathbf{B}^k = \Sigma_k + \mathbf{U}_k \mathbf{U}_k^\top,$$

where $\mathbf{U}_k = [\mathbf{u}_{k-1}^{\kappa(k,1)} \ \mathbf{u}_{k-2}^{\kappa(k,2)} \ \dots \ \mathbf{u}_{k-K_s}^{\kappa(k,K_s)}] \in \mathbb{R}^{N \times K_s}$ and $\Sigma_k = \tau_k \mathbf{I}_N$ with $\tau_k = \sum_{t=1}^{K_s} \tau_{k-t}^{\kappa(k,t)}$. Using the Woodbury matrix identity, we obtain

$$(\mathbf{B}^k)^{-1} = (\tau_k)^{-1} \mathbf{I}_N - (\tau_k)^{-2} \mathbf{U}_k (\mathbf{I}_{K_s} + \frac{\mathbf{U}_k^\top \mathbf{U}_k}{\tau_k})^{-1} \mathbf{U}_k^\top,$$

so that $(\mathbf{B}^k)^{-1}$ is easily applied.

To compute $\text{prox}_{\delta_C}^{\mathbf{B}^k} (\mathbf{x})$, we use Theorem 1, which requires solving a nonsmooth and nonlinear system of equations similar to (10). Since K_s is small, we solve it using a semi-smooth Newton method [44]. Let

$$\text{dom}_\varphi = \{\beta \in \mathbb{R}^{K_s} \mid \varphi(\beta) \text{ is differentiable at } \beta\}.$$

Then, the generalized Jacobian of φ at β is defined by

$$\partial \varphi(\beta) = \text{conv } \partial_{\text{dom}_\varphi} \varphi(\beta),$$

where $\partial_{\text{dom}_\varphi} \varphi(\beta) = \left\{ \lim_{\substack{\beta_k \rightarrow \beta \\ \beta_k \in \text{dom}_\varphi}} \varphi(\beta_k) \right\}$ and conv denotes a convex hull. With these definitions, at the k th iteration, the semi-smooth Newton method [44] updates β_k through

$$\beta_k = \beta_{k-1} - \mathbf{H}_{k-1}^{-1} \varphi(\beta_{k-1}),$$

where $\mathbf{H}_{k-1} \in \partial\varphi(\beta_{k-1})$. Algorithm 4 presents the implementation details of the semi-smooth Newton method. In our experiments, Algorithm 4 reaches a small error tolerance (e.g., 10^{-6}) after few iterations.

Algorithm 4 Semi-smooth Newton to solve $\varphi(\beta) = \mathbf{0}$

Initialization:

Initial guess β_0 ; tolerance ϵ (e.g., 10^{-6}); maximal number of iterations Max_Iter.

Output: β^*

- 1: $k \leftarrow 1$
- 2: **for all** $k \leq \text{Max_Iter}$ **do**
- 3: **if** $\|\varphi(\beta_{k-1})\|_2 \leq \epsilon$ **then**
- 4: **return**
- 5: **else**
- 6: Pick $\mathbf{H}_{k-1} \in \partial\varphi(\beta_{k-1})$ and run

$$\beta_k = \beta_{k-1} - \mathbf{H}_{k-1}^{-1}\varphi(\beta_{k-1})$$

- 7: **end if**
 - 8: $k \leftarrow k + 1$
 - 9: **end for**
 - 10: **return** $\beta^* = \beta_k$.
-

V. NUMERICAL EXPERIMENTS

Optical diffraction tomography (ODT) is a noninvasive and label-free technique that allows one to obtain a refractive-index (RI) map of the sample [46]. In ODT, the sample is sequentially illuminated from different angles. The outgoing complex wave field of each illumination is recorded through a digital-holography microscope [47]. Finally, the RI map is recovered by solving an inverse-scattering problem. We display a scheme of the acquisition principle in Fig. 2.

ODT is ideal for studying the performance of BQNPM. Indeed, inverse-scattering problems are composite minimization problems and can be convex or nonconvex, depending on the choice of a linear or nonlinear physical model. For further details about ODT, we refer the reader to [2] and the references therein.

We study the performance of BQNPM to reconstruct the RI map with simulated and real data using an isotropic TV regularizer and nonnegative constraints. Specifically, we solve

$$\mathbf{x}^* \in \arg \min_{\mathbf{x} \in \mathbb{R}_+^N} \Phi(\mathbf{x}), \quad (21)$$

where $\Phi(\mathbf{x}) \equiv \left(\frac{1}{L} \sum_{\varrho=1}^L \frac{1}{2} \|\mathcal{H}_{\varrho}(\mathbf{x}) - \mathbf{y}_{\varrho}\|_2^2 + \lambda \text{TV}_{\text{iso}}(\mathbf{x}) \right)$ and the forward imaging model is nonlinear, based on the Lippmann-Schwinger (LippS) equation [2]. This physical mapping is accurate for strongly scattering samples. However, this comes at the price of a computationally demanding model. For completeness, we describe the details of $\mathcal{H}_{\varrho}(\cdot)$ in the supplementary material. For both simulated and real data, we compare BQNPM with ASPM² and the stochastic quasi-Newton proximal method (SQNPM) proposed in [41]. SQNPM is guaranteed to converge under the Kurdyka-Łojasiewicz condition. Note that Wang *et al.* [41] only

²The complete steps of ASPM are provided in the supplementary material.

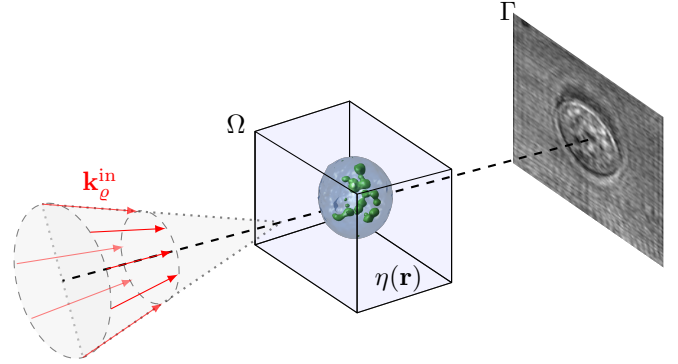


Fig. 2. Principle of optical diffraction tomography. The arrows represent the wave vectors $\{\mathbf{k}_{\varrho}^{\text{in}} \in \mathbb{R}^3\}_{\varrho=1}^L$ of the L incident plane waves $\{u_{\text{in}}^{\varrho}\}_{\varrho=1}^L$. The angles of illumination are limited to a cone around the optical axis. The refractive-index map of the sample $\eta(\mathbf{r})$ is embedded in the domain $\Omega \subset \mathbb{R}^3$, and the recorded domain is denoted by Γ .

considered $g(\mathbf{x}) = \|\mathbf{x}\|_1$, but, for the sake of fairness, we consider a constrained-TV regularization instead. We then deploy Algorithm 2 to efficiently solve the related WPM. In consequence, we only compare the Hessian estimation approach of [41] with ours.

For the simulated data, we first recover RI maps using the first-order Born approximation [48]. The corresponding physical model is then linear, which makes (21) a convex optimization problem. This favorable setting allows us to study more thoroughly the behavior of BQNPM. We then recover RI maps using LippS on simulated and real data, which means that (21) now corresponds to a nonconvex optimization problem.

All experiments are run on a workstation with 3.3GHz AMD EPYC 7402 and NVIDIA GeForce RTX 3090. For a fair comparison, all reconstruction algorithms are run on the same GPU platform. Our implementation is based on the GlobalBioIm library [49].

A. Simulated Data

Simulation Settings: We mainly use two phantoms as the ground-truth volumes: one weakly scattering sample (maximal RI 1.363) and one strongly scattering sample (maximal RI 1.43). The weakly scattering sample with RI $\eta_{\text{weak}}(\mathbf{r})$ is immersed in a medium with RI $\eta_{\text{m}} = 1.333$ and is illuminated by plane waves of wavelength $\lambda_{\text{in}} = 406\text{nm}$. The domain Ω is a cube of edge length $3.2\mu\text{m}$ and fully contains the sample. To obtain the complex-valued measurements, we use the first-order Born approximation on a grid with a resolution of 50nm, which results in a total of 64^3 voxels to discretize Ω and η_{weak} . The sample is probed by $L = 60$ tilted plane waves $u_{\text{in}}^{\varrho}(\mathbf{r}) = \exp(j\mathbf{k}_{\varrho}^{\text{in}} \cdot \mathbf{r})$ for $\varrho = 1, \dots, L$. The wavevectors $\{\mathbf{k}_{\varrho}^{\text{in}} \in \mathbb{R}^3\}_{\varrho=1}^L$ are embedded in a cone with half-angle 42° (Fig. 2). We then obtain a total of 60×512^2 measurements. Without the regularization, this setting makes our inverse problem ill-posed. The measurements are lacking information on the frequency along the optical axis, *i.e.*, the so-called missing cone problem. For the strongly scattering

sample, we proceed similarly (same medium and wavelength) but simulate with the LippS model to generate the measurements instead. To study further the convergence property of BQNPM, in Section V-A4, we use the proposed method to recover strongly scattering sample with different contrasts to show its fast convergence.

1) *Linear Model–Weakly Scattering Sample*: The tradeoff parameter $\lambda = 10/64^3$ is optimized by grid search and the stepsize is set to 0.1. BQNPM with the parameters $a_k = 1$ and $\gamma = 0.8$ performed well for our experiments. We have a total of $K_s = 4$ subsets ($\{\mathcal{S}_t\}_{t=1}^4$ with fifteen measurement images each). Note that the fifteen illumination angles are equally spaced.³ 100 iterations are performed to recover the RI maps. The Rytov approximation (closed-form solution) is used as the initial guess for ASPM, SQNPM [41], and BQNPM.

The first row of Fig. 3 contain the full cost with respect to iterations and the wall time of ASPM, SQNPM, and BQNPM. We see that BQNPM converges faster than ASPM in terms of iterations and wall time. The computational cost per iteration for BQNPM is similar to that of ASPM, which indicates that the computational overhead of WPM is negligible. In the first twenty iterations, SQNPM reaches the lowest full cost among the three algorithms. However, BQNPM outpaces SQNPM after 22 iterations. From Fig. 3(b), BQNPM converges as well as SQNPM in terms of wall time, even in the first iterations. This is because SQNPM requires computing the full gradient every K_s iterations, whereas BQNPM never computes the full gradient. Note that the gradient computation in the linear Born model is relatively inexpensive. Yet, BQNPM performs similarly than SQNPM. In the next experiments, this gradient computation will become significantly more expensive because of the deployment of the nonlinear LippS model.

From the second row of Fig. 3, we see that BQNPM requires less wall time than ASPM and SQNPM to reach the highest SNR, which corroborates our previous observations. Moreover, ASPM (respectively, SQNPM) needs 100 iterations, 267.5 seconds (respectively, 283.5 seconds), to reach its highest SNR while BQNPM only requires 34 iterations (99.7 seconds) to get a comparable SNR. Note that BQNPM slightly increases the full cost when it first uses second-order information. In our experiments, we consistently observe that BQNPM increases the full cost at $K_s + 1$ th iteration, which coincides with the first time we used the second-order information, *i.e.*, Steps 8-10 in Algorithm 1. This behavior might be due to an inaccurate estimation of the Hessian in the first iterations.

In Fig. 4, we display the orthoviews of the RI maps obtained with ASPM, SQNPM, and BQNPM at the 100th, 100th, and 34th iteration, respectively. Here, we see that the first-order Born approximation is accurate for the weakly scattering sample.

2) *Nonlinear LippS Model–Strongly Scattering Sample*: In this part, we study the performance of BQNPM to recover the RI maps using the LippS model.⁴ The regularization λ and

³We also tried to choose the illumination angles randomly for ASPM but found that selecting them in equally spaced yields slightly better performance.

⁴The reconstruction of a strongly scattering sample with a linear model is presented in the supplementary material. There, we clearly see the advantages of an accurate model.

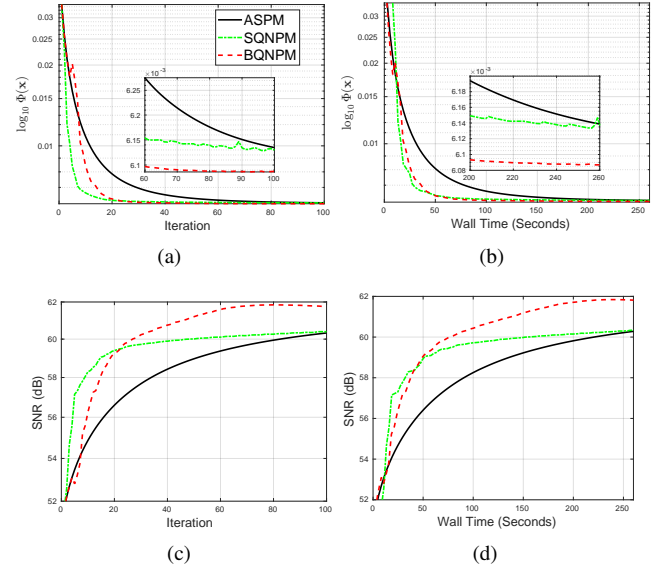


Fig. 3. Performance of ASPM, SQNPM [41], and BQNPM algorithms on the weakly scattering simulated sample using the first-order Born approximation. From top to bottom rows: Full cost ($\Phi(\mathbf{x}_k)$) and SNR with respect to iteration and wall time, respectively.

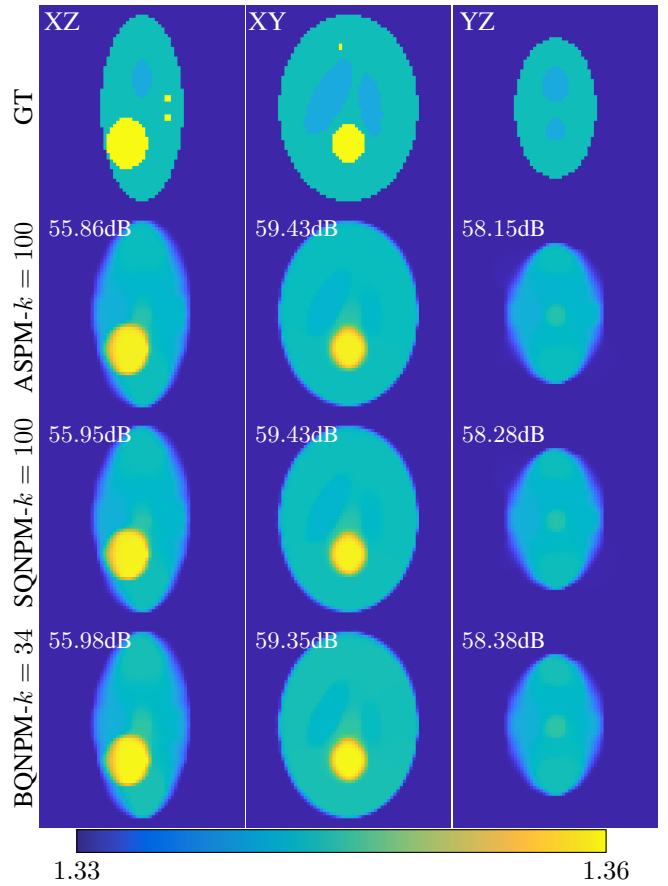


Fig. 4. Orthoviews of the 3D refractive index maps obtained by ASPM (iter. $k = 100$), SQNPM [41] (iter. $k = 100$) and BQNPM (iter. $k = 34$) algorithms on the weakly scattering simulated sample using the first-order Born approximation. The SNR for each slice is displayed in the top-left corner of each image.

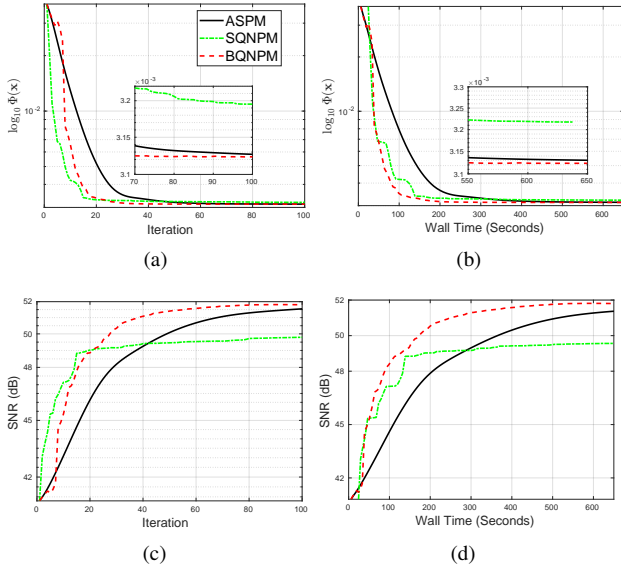


Fig. 5. Performance of ASPM, SQNPM [41], and BQNPM algorithms on the strongly scattering simulated sample using the LippS model. From top to bottom rows: Full cost and SNR with respect to iteration and wall time.

the stepsize are set as $1/64^3$ and $1/200$, respectively. A total of 100 iterations are run for ASPM, SQNPM, and BQNPM.

In Fig. 5, we show the evolution of the full cost and SNR with respect to the iterations and wall time for the three algorithms. Although SQNPM converges faster than other two algorithms in terms of iteration at the beginning, it becomes slower than BQNPM after 20 iterations. Moreover, BQNPM requires fewer iterations than ASPM to reach a lower full cost and BQNPM is the fastest algorithm in terms of wall time. From the second row of Fig. 5, we observe that BQNPM obtains a higher SNR than ASPM and SQNPM in a shorter time. In Fig. 6, we display the orthoviews of the RI maps recovered by ASPM, SQNPM, and BQNPM. We can see that ASPM achieves the highest SNR at the 100th iteration (767.6 seconds) while BQNPM only requires 59 iterations (393.2 seconds) to achieve a similar SNR. All these results for a nonconvex composite-optimization problem corroborate the observations we made on the convex counterpart.

3) *On the Choice of K_s and γ* : In this part, we study the influence of K_s and γ on the convergence of BQNPM. We present in Fig. 7 the full cost with respect to iterations for different values of K_s . The convergence of BQNPM is influenced by the value of K_s . In particular, a smaller K_s yields faster convergence, because a smaller K_s yields a more accurate gradient and Hessian estimation. Indeed, $K_s = 1$ is the fastest setting in terms of iteration since it uses the full gradient at each iteration. However, BQNPM with $K_s = 1$ requires more computation at each iteration and thus loses its efficiency in terms of wall time. Indeed, from Fig. 7(b), we clearly see that BQNPM with $K_s = 1$ is slower than $K_s \neq 1$ in terms of wall time.

BQNPM slightly increases the full cost when it starts to use second-order information (line 8 in Algorithm 1), but then immediately reduces it in subsequent iterations. As previously observed, the full cost is consistently increased at the $K_s + 1$ th

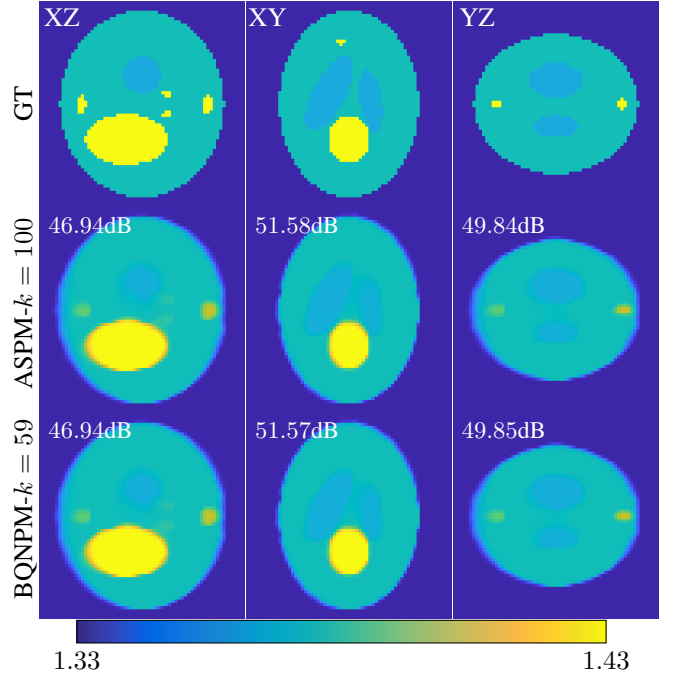


Fig. 6. Orthoviews of the 3D refractive-index maps obtained by ASPM (iter. $k = 100$) and BQNPM (iter. $k = 59$) algorithms on the strongly scattering simulated sample using the Lippmann-Schwinger model. The SNR for each slice is displayed in the top-left corner of each image.

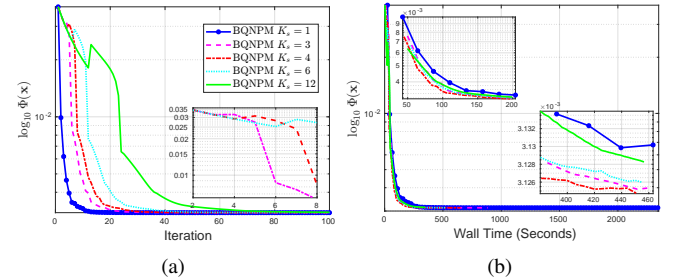


Fig. 7. Influence of K_s on the convergence of BQNPM with $\gamma = 0.8$.

iteration (Fig. 7(a)). In this work, we choose $K_s = 4$ (i.e., 15 measurements per subset). Fig. 8 describes the effect of γ on the convergence of BQNPM. We see that BQNPM exhibits a low sensitivity to γ . Yet, as $\gamma = 0.8$ still yields slightly better results, we choose $\gamma = 0.8$ in our experiments.

Fig. 9 presents the memory usage of different algorithms for various K_s . Note that we use command 'nvidia-smi' to measure the memory usage at $2K_s + 1$ th iteration for each algorithm. For ASPM and SQNPM, we observe that the extra memory for large K_s is negligible. By contrast, BQNPM needs more memory. In fact, the measured memory usage is much higher than expected, as BQNPM needs to store $3K_s$ additional images (Algorithm 1). This gap is probably due to the current implementation which does not optimize the memory usage.

4) *Convergence Study on Different Contrast Samples*: To study the convergence of BQNPM, we compare the reconstruction performance of ASPM, SQNPM, and BQNPM

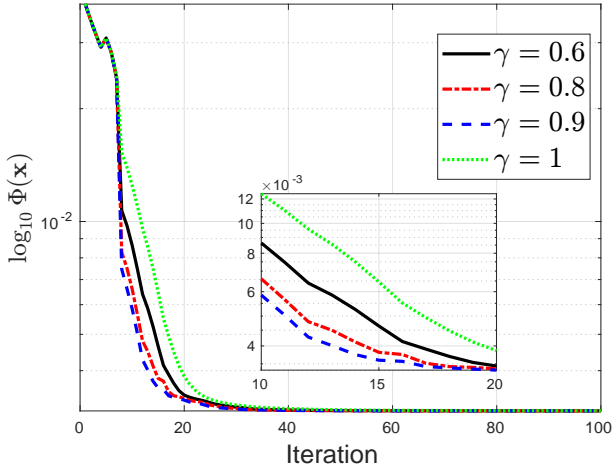


Fig. 8. Influence of γ on the convergence of BQNPM.

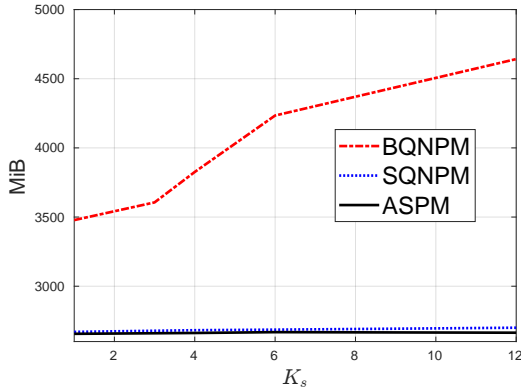


Fig. 9. Memory usage of ASPM, SQNPM, and BQNPM for different K_s with same experimental setting as Fig. 5.

on various samples with different maximal RI (denoted by η_{\max}). The algorithmic setting used here is identical to Fig. 5. Table II reports the experimental results. As described in the supplementary material, the LippS model requires to solve the Lippmann-Schwinger equation and a high RI sample results in slower convergence for solving the Lippmann-Schwinger equation [50]. Indeed, from Table II, we see that ASPM requires more wall time to run 100 iterations when the maximal RI is increased. Moreover, we observe that BQNPM is 2 ~ 3 time faster than ASPM to obtain a higher SNR for various settings. These results illustrate well the fast convergence of our approach. In this experimental setting, SQNPM cannot obtain a higher SNR than ASPM with the same number of iterations, which corroborates the observation in Fig. 5.

B. Real Data

Finally, we assess the performance of the proposed method on real data of a yeast cell immersed in water ($\eta_m = 1.338$). The sample was illuminated by 60 incident plane waves ($\lambda = 532\text{nm}$) embedded in a cone of illumination whose half-angle is 35° [9, 51]. The discretized volume has a total of 96^3 voxels of size 99^3nm^3 . We refer the reader to [2, 9, 51] for the detailed description of the acquisition setting. The stepsize and regularization parameter are set as 0.01 and

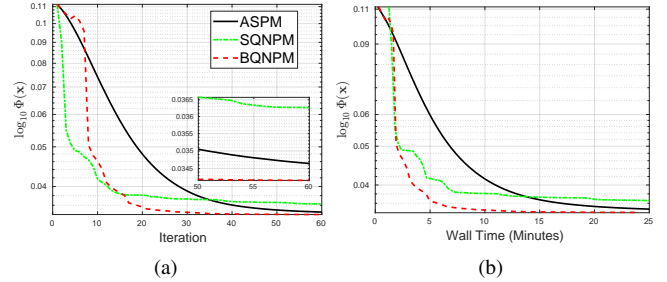


Fig. 10. Full cost with respect to iteration and wall time for ASPM, SQNPM, and BQNPM on real data (yeast cell) using the LippS model.

$2/96^3$, respectively. Moreover, 60×150^2 measurements are used for the reconstruction and 60 iterations are run for ASPM and BQNPM. We display in Fig. 10 the evolution of the full cost for both algorithms. Similarly to the simulated cases, we see that BQNPM requires fewer iterations and wall time to achieve a lower full cost. We further compare the orthoviews of the RI maps obtained at the 10th, 30th, 40th, and 50th iteration in Fig. 11. We see that BQNPM recovers a qualitatively good RI map in 30 iterations (627.2 seconds), while ASPM achieves a similar quality only after 50 iterations (1338.8 seconds). In [9], the reconstructed images of the same yeast cell are similar to the images obtained by our method.

VI. CONCLUSIONS

We have proposed a mini-batch quasi-Newton proximal method (BQNPM) to solve constrained total-variation-based image reconstruction problems. The computational cost of BQNPM does not depend on the number of measurements, which makes it suitable for composite-minimization problems with many sets of measurements. In addition, our method does not require the computation of the full gradient of the data-fidelity term, thus avoiding the costly step of a traverse of the entire set of measurements. This is a major departure from existing stochastic proximal quasi-Newton methods. We have also proposed an efficient method to compute the weighted proximal mapping that arises in BQNPM. Our numerical experiments on 3D optical-diffraction tomography with simulated and real data show that BQNPM converges more rapidly than a stochastic accelerated first-order proximal method in terms of iterations and wall time. These results illustrate how the computational cost of composite inverse problems can be significantly reduced by the proposed method.

ACKNOWLEDGEMENTS

The authors would like to thank Dr. Ahmed Ayoub, Dr. Joowon Lim, and Prof. Demetri Psaltis for providing us with real data.

APPENDIX A PROOF OF LEMMA 1

Proof. Denote by $\mathbf{H}_C(\mathbf{x}) = \mathbf{x} - \text{prox}_{\delta_c}^{\mathbf{B}^k}(\mathbf{x})$ and $h(\mathbf{P}) = \left(-\|\mathbf{H}_C(\mathbf{w}(\mathbf{P}))\|_{\mathbf{B}^k}^2 + \|\mathbf{w}(\mathbf{P})\|_{\mathbf{B}^k}^2 \right)$. Using (8) and the chain

TABLE II

CONVERGENCE STUDY OF ASPM, SQNPM, AND BQNPM ON THE RECONSTRUCTION OF STRONGLY SCATTERING SAMPLES WITH DIFFERENT MAXIMAL RI. ASPM RUNS 100 ITERATIONS AS A BENCHMARK. THE NUMBER OF ITERATIONS AND CORRESPONDING WALL TIME OF SQNPM AND BQNPM WHICH FIRST YIELD A HIGHER SNR THAN ASPM ARE USED TO MEASURE THE CONVERGENCE SPEED. “-” MEANS THE METHOD COULD NOT OBTAIN HIGHER SNR THAN ASPM IN 100 ITERATIONS.

Methods	η_{\max} 1.41		1.42		1.44		1.45		1.47		1.49		1.51		1.53	
	iter.↓	sec.↓	iter.↓	sec.↓	iter.↓	sec.↓	iter.↓	sec.↓	iter.↓	sec.↓	iter.↓	sec.↓	iter.↓	sec.↓	iter.↓	sec.↓
ASPM	100	702.2	100	736.9	100	815.6	100	853.5	100	952.6	100	1068.2	100	1199.8	100	1338.8
SQNPM	-	-	-	-	-	-	-	-	-	-	-	-	-	-	-	-
BQNPM	57	363.0	51	338.2	44	317.5	41	305.8	36	289.2	34	301.4	34	332.2	34	366.6

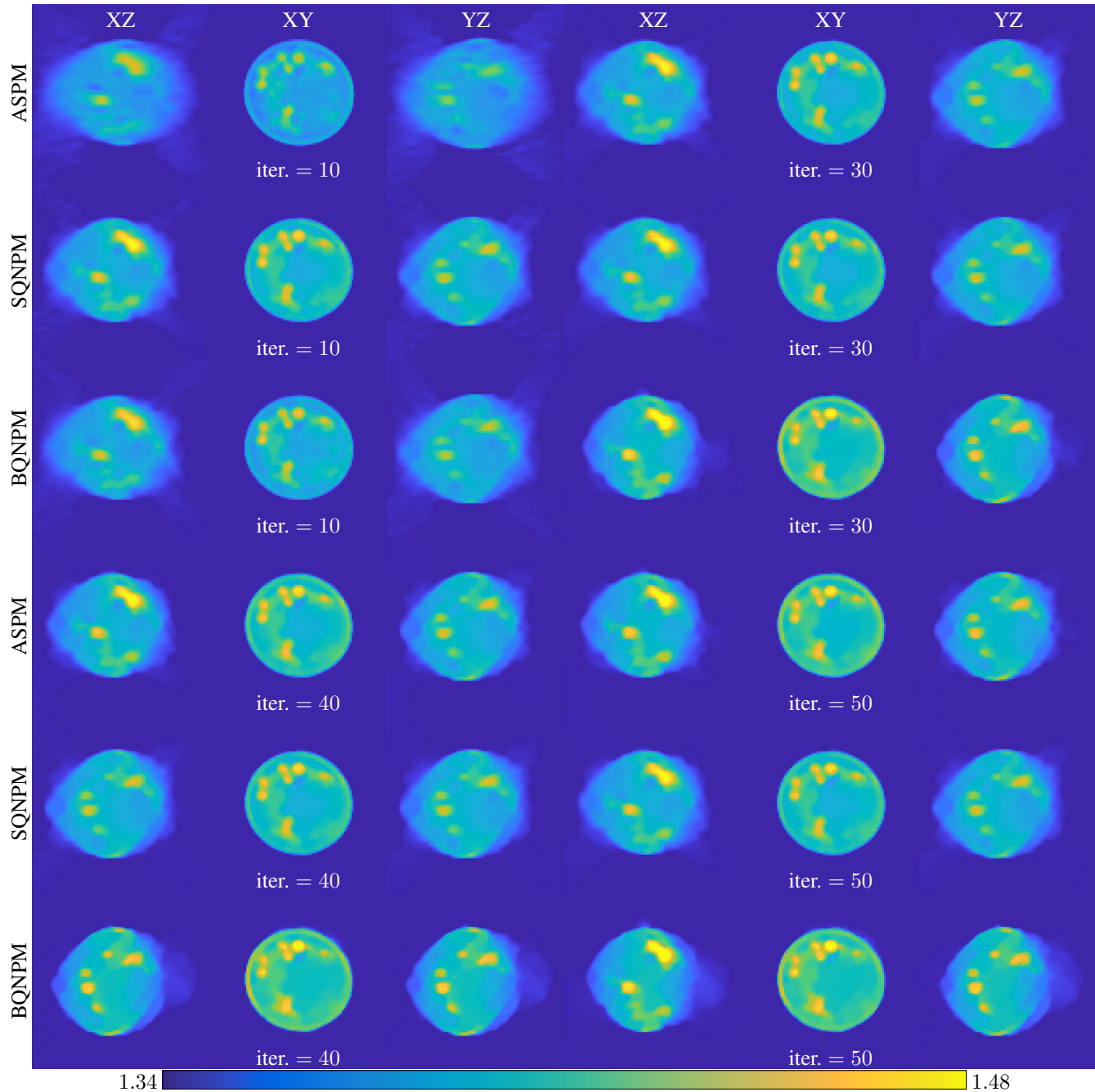


Fig. 11. Reconstructions of ASPM, SQNPM, and BQNPM algorithms on real data (yeast cell) using the Lippmann-Schwinger model. Orthoviews of the 3D refractive-index maps obtained by ASPM, SQNPM, and BQNPM at the 10th, 30th, 40th, and 50th iterations.

rule, we have that $\nabla \|\mathbf{H}_C(\mathbf{x})\|_{\mathbf{B}^k}^2 = 2\mathbf{B}^k \mathbf{H}_C(\mathbf{x})$. Then the gradient of $h(\mathbf{P})$ is

$$\begin{aligned} \nabla h(\mathbf{P}) &= 2a_k K_s \lambda \mathbf{d} \left(\mathbf{H}_C(\mathbf{w}(\mathbf{P})) - \mathbf{w}(\mathbf{P}) \right) \\ &= -2a_k K_s \lambda \mathbf{d} \left(\text{prox}_{\delta_c}^{\mathbf{B}^k}(\mathbf{w}(\mathbf{P})) \right). \end{aligned} \quad (22)$$

Now, we compute the Lipschitz constant of $h(\mathbf{P})$. For every two pairs of (\mathbf{P}_1) and (\mathbf{P}_2) , we have that

$$\begin{aligned} &\|\nabla h(\mathbf{P}_1) - \nabla h(\mathbf{P}_2)\| \\ &= \left\| 2a_k K_s \lambda \mathbf{d} \left(\text{prox}_{\delta_c}^{\mathbf{B}^k}(\mathbf{w}(\mathbf{P}_1)) - \text{prox}_{\delta_c}^{\mathbf{B}^k}(\mathbf{w}(\mathbf{P}_2)) \right) \right\| \\ &\stackrel{(*)}{\leq} 2a_k K_s \lambda \sqrt{\omega_{\min}^k} \|\mathbf{d}\| \cdot \|T a_k \lambda (\mathbf{B}^k)^{-1} (\mathbf{d}^\top(\mathbf{P}_1) \\ &\quad - \mathbf{d}^\top(\mathbf{P}_2))\|_{\mathbf{B}^k} \\ &\stackrel{(**)}{\leq} 2\omega_{\min}^k a_k^2 T^2 \lambda^2 \|\mathbf{d}\| \cdot \|\mathbf{d}^\top\| \cdot \|(\mathbf{P}_1) - (\mathbf{P}_2)\| \\ &= 2\omega_{\min}^k a_k^2 T^2 \lambda^2 \|\mathbf{d}\|^2 \cdot \|(\mathbf{P}_1) - (\mathbf{P}_2)\|, \end{aligned} \quad (23)$$

where the transition $(*)$ follows from the non-expansiveness property of the WPM [19], while $(**)$ follows from the fact that $\|(\mathbf{B}^k)^{-1} \mathbf{x}\|_{\mathbf{B}^k} \leq \sqrt{\omega_{\min}^k} \|\mathbf{x}\|$, with ω_{\min}^k the smallest eigenvalue of (\mathbf{B}^k) . In 2D, we have that $\|\mathbf{d}\| = \sqrt{8}$ (see the proof of [15, Lemma 4.2]). In 3D, we similarly obtain that $\|\mathbf{d}\| = \sqrt{12}$. The Lipschitz constant of $h(\mathbf{P})$ is then $16\omega_{\min}^k a_k^2 T^2 \lambda^2$ ($24\omega_{\min}^k a_k^2 T^2 \lambda^2$) for 2D (3D). We note that ω_{\min}^k can be obtained through the power method since $(\mathbf{B}^k)^{-1} \mathbf{x}$ can be applied cheaply in our case. Alternatively, one could adopt a backtracking strategy to search the stepsize at each iteration [43]. \square

REFERENCES

- [1] F. D. M. Neto and A. J. da Silva Neto, *An Introduction to Inverse Problems with Applications*. Springer Science & Business Media, 2012.
- [2] T.-a. Pham, E. Soubies, A. Ayoub, J. Lim, D. Psaltis, and M. Unser, “Three-dimensional optical diffraction tomography with Lippmann-Schwinger model,” *IEEE Transactions on Computational Imaging*, vol. 6, pp. 727–738, 2020.
- [3] L. Métivier, R. Brossier, J. Virieux, and S. Operto, “Full waveform inversion and the truncated Newton method,” *SIAM Journal on Scientific Computing*, vol. 35, no. 2, pp. B401–B437, 2013.
- [4] L. I. Rudin, S. Osher, and E. Fatemi, “Nonlinear total variation based noise removal algorithms,” *Physica D: Nonlinear Phenomena*, vol. 60, no. 1-4, pp. 259–268, 1992.
- [5] S. Lefkimmatis, J. P. Ward, and M. Unser, “Hessian Schatten-norm regularization for linear inverse problems,” *IEEE Transactions on Image Processing*, vol. 22, no. 5, pp. 1873–1888, 2013.
- [6] D. Ulyanov, A. Vedaldi, and V. Lempitsky, “Deep image prior,” in *Proceedings of the IEEE Conference on Computer Vision and Pattern Recognition*, 2018, pp. 9446–9454.
- [7] S. V. Venkatakrisnan, C. A. Bouman, and B. Wohlberg, “Plug-and-play priors for model based reconstruction,” in *Global Conference on Signal and Information Processing (GlobalSIP), 2013 IEEE*. IEEE, 2013, pp. 945–948.
- [8] Y. Romano, M. Elad, and P. Milanfar, “The little engine that could: Regularization by denoising (RED),” *SIAM Journal on Imaging Sciences*, vol. 10, no. 4, pp. 1804–1844, 2017.
- [9] J. Lim, A. B. Ayoub, E. E. Antoine, and D. Psaltis, “High-fidelity optical diffraction tomography of multiple scattering samples,” *Light: Science & Applications*, vol. 8, no. 1, p. 82, 2019.
- [10] S. Chowdhury, M. Chen, R. Eckert, D. Ren, F. Wu, N. Repina, and L. Waller, “High-resolution 3D refractive index microscopy of multiple-scattering samples from intensity images,” *Optica*, vol. 6, no. 9, pp. 1211–1219, 2019.
- [11] A. Chambolle, S. E. Levine, and B. J. Lucier, “An upwind finite-difference method for total variation-based image smoothing,” *SIAM Journal on Imaging Sciences*, vol. 4, no. 1, pp. 277–299, 2011.
- [12] A. Chambolle, “An algorithm for total variation minimization and applications,” *Journal of Mathematical Imaging and Vision*, vol. 20, no. 1, pp. 89–97, 2004.
- [13] D. Goldfarb and W. Yin, “Second-order cone programming methods for total-variation-based image restoration,” *SIAM Journal on Scientific Computing*, vol. 27, no. 2, pp. 622–645, 2005.
- [14] T. Chan, S. Esedoglu, F. Park, and A. Yip, “Total variation image restoration: Overview and recent developments,” *Handbook of Mathematical Models in Computer Vision*, pp. 17–31, 2006.
- [15] A. Beck and M. Teboulle, “Fast gradient-based algorithms for constrained total variation image denoising and deblurring problems,” *IEEE Transactions on Image Processing*, vol. 18, no. 11, pp. 2419–2434, 2009.
- [16] J. Nocedal and S. J. Wright, *Numerical Optimization*. Springer, 2006.
- [17] M. Schmidt, E. Berg, M. Friedlander, and K. Murphy, “Optimizing costly functions with simple constraints: A limited-memory projected quasi-Newton algorithm,” in *Artificial Intelligence and Statistics*, 2009, pp. 456–463.
- [18] D. Kim, S. Sra, and I. S. Dhillon, “Tackling box-constrained optimization via a new projected quasi-Newton approach,” *SIAM Journal on Scientific Computing*, vol. 32, no. 6, pp. 3548–3563, 2010.
- [19] J. D. Lee, Y. Sun, and M. A. Saunders, “Proximal Newton-type methods for minimizing composite functions,” *SIAM Journal on Optimization*, vol. 24, no. 3, pp. 1420–1443, 2014.
- [20] S. Karimi and S. Vavasis, “IMRO: A proximal quasi-Newton method for solving ℓ_1 -regularized least squares problems,” *SIAM Journal on Optimization*, vol. 27, no. 2, pp. 583–615, 2017.
- [21] S. Becker, J. Fadili, and P. Ochs, “On quasi-Newton forward-backward splitting: Proximal calculus and convergence,” *SIAM Journal on Optimization*, vol. 29, no. 4, pp. 2445–2481, 2019.

- [22] T. Hong, I. Yavneh, and M. Zibulevsky, "Solving RED with weighted proximal methods," *IEEE Signal Processing Letters*, vol. 27, pp. 501–505, 2020.
- [23] T. Ge, U. Villa, U. S. Kamilov, and J. A. O'Sullivan, "Proximal Newton methods for x-ray imaging with non-smooth regularization," *Electronic Imaging*, no. 14, pp. 7–1, 2020.
- [24] T. Hong, L. Hernandez-Garcia, and J. A. Fessler, "A complex quasi-Newton proximal method for image reconstruction in compressed sensing MRI," *IEEE Transactions on Computational Imaging*, vol. 10, pp. 372 – 384, Feb. 2024.
- [25] A. Kadu, H. Mansour, and P. T. Boufounos, "High-contrast reflection tomography with total-variation constraints," *IEEE Transactions on Computational Imaging*, vol. 6, pp. 1523–1536, 2020.
- [26] E. Chouzenoux, J.-C. Pesquet, and A. Repetti, "Variable metric forward–backward algorithm for minimizing the sum of a differentiable function and a convex function," *Journal of Optimization Theory and Applications*, vol. 162, no. 1, pp. 107–132, 2014.
- [27] S. Bonettini, I. Loris, F. Porta, and M. Prato, "Variable metric inexact line-search-based methods for nonsmooth optimization," *SIAM Journal on Optimization*, vol. 26, no. 2, pp. 891–921, 2016.
- [28] A. Repetti and Y. Wiaux, "Variable metric forward-backward algorithm for composite minimization problems," *SIAM Journal on Optimization*, vol. 31, no. 2, pp. 1215–1241, 2021.
- [29] L. Bottou, "Large-scale machine learning with stochastic gradient descent," in *Proceedings of COMPSTAT'2010: 19th International Conference on Computational Statistics Paris France, August 22-27, 2010 Keynote, Invited and Contributed Papers*. Springer, 2010, pp. 177–186.
- [30] R. Johnson and T. Zhang, "Accelerating stochastic gradient descent using predictive variance reduction," *Advances in neural information processing systems*, vol. 26, 2013.
- [31] A. Defazio, F. Bach, and S. Lacoste-Julien, "Saga: A fast incremental gradient method with support for non-strongly convex composite objectives," *Advances in Neural Information Processing Systems*, vol. 27, 2014.
- [32] M. Schmidt, N. Le Roux, and F. Bach, "Minimizing finite sums with the stochastic average gradient," *Mathematical Programming*, vol. 162, pp. 83–112, 2017.
- [33] E. Chouzenoux and J.-C. Pesquet, "A stochastic majorize-minimize subspace algorithm for online penalized least squares estimation," *IEEE Transactions on Signal Processing*, vol. 65, no. 18, pp. 4770–4783, 2017.
- [34] E. Soubies, T.-a. Pham, and M. Unser, "Efficient inversion of multiple-scattering model for optical diffraction tomography," *Optics Express*, vol. 25, no. 18, pp. 21 786–21 800, 2017.
- [35] P. Moritz, R. Nishihara, and M. Jordan, "A linearly-convergent stochastic L-BFGS algorithm," in *Artificial Intelligence and Statistics*. PMLR, 2016, pp. 249–258.
- [36] N. Agarwal, B. Bullins, and E. Hazan, "Second-order stochastic optimization for machine learning in linear time," *The Journal of Machine Learning Research*, vol. 18, no. 1, pp. 4148–4187, 2017.
- [37] X. Wang, S. Ma, D. Goldfarb, and W. Liu, "Stochastic quasi-Newton methods for nonconvex stochastic optimization," *SIAM Journal on Optimization*, vol. 27, no. 2, pp. 927–956, 2017.
- [38] D. Goldfarb, Y. Ren, and A. Bahamou, "Practical quasi-Newton methods for training deep neural networks," *Advances in Neural Information Processing Systems*, vol. 33, pp. 2386–2396, 2020.
- [39] F. Curtis, "A self-correcting variable-metric algorithm for stochastic optimization," in *International Conference on Machine Learning*. PMLR, 2016, pp. 632–641.
- [40] M. Yang, A. Milzarek, Z. Wen, and T. Zhang, "A stochastic extra-step quasi-Newton method for nonsmooth non-convex optimization," *Mathematical Programming*, pp. 1–47, 2021.
- [41] X. Wang, X. Wang, and Y.-X. Yuan, "Stochastic proximal quasi-Newton methods for non-convex composite optimization," *Optimization Methods and Software*, vol. 34, no. 5, pp. 922–948, 2019.
- [42] N. Parikh and S. Boyd, "Proximal algorithms," *Foundations and Trends in Optimization*, vol. 1, no. 3, pp. 127–239, 2014.
- [43] A. Beck, *First-Order Methods in Optimization*. SIAM, 2017.
- [44] L. Qi and D. Sun, "A survey of some nonsmooth equations and smoothing Newton methods," in *Progress in Optimization*. Springer, 1999, pp. 121–146.
- [45] A. Mokhtari, M. Eisen, and A. Ribeiro, "IQN: An incremental quasi-Newton method with local superlinear convergence rate," *SIAM Journal on Optimization*, vol. 28, no. 2, pp. 1670–1698, 2018.
- [46] E. Wolf, "Three-dimensional structure determination of semi-transparent objects from holographic data," *Optics Communications*, vol. 1, no. 4, pp. 153–156, 1969.
- [47] M. K. Kim, "Principles and techniques of digital holographic microscopy," *SPIE Reviews*, vol. 1, no. 1, p. 018005, 2010.
- [48] B. Chen and J. J. Stamnes, "Validity of diffraction tomography based on the first Born and the first Rytov approximations," *Applied Optics*, vol. 37, no. 14, pp. 2996–3006, 1998.
- [49] E. Soubies, F. Soulez, M. McCann, T.-a. Pham, L. Donati, T. Debarre, D. Sage, and M. Unser, "Pocket guide to solve inverse problems with GlobalBioIm," *Inverse Problems*, vol. 35, no. 10, pp. 1–20, 2019.
- [50] T. Hong, T.-a. Pham, E. Treister, and M. Unser, "Diffraction tomography with Helmholtz equation: Efficient and robust multigrid-based solver," *arXiv preprint arXiv:2107.03679*, 2021.
- [51] A. B. Ayoub, T.-A. Pham, J. Lim, M. Unser, and D. Psaltis, "A method for assessing the fidelity of optical diffraction tomography reconstruction methods using structured illumination," *Optics Communications*, p. 124486, 2019.